

Featuring research from the Department of Biosystems Research and Development at Sandia National Laboratories, Livermore, California.

Title: Isotropically etched radial micropore for cell concentration, immobilization, and picodroplet generation

Using an adaptation of single-level isotropic wet etching, small shallow micropores are radially embedded in larger deeper microchannels for cell concentration, immobilization, and picodroplet generation.

As featured in:



See Kamlesh D. Patel *et al.*, *Lab Chip*, 2009, **9**, 507–515

RSC Publishing

www.rsc.org

Registered Charity Number 207890

# Isotropically etched radial micropore for cell concentration, immobilization, and picodroplet generation†

Thomas D. Perroud, Robert J. Meagher, Michael P. Kanouff, Ronald F. Renzi, Meiye Wu, Anup K. Singh and Kamlesh D. Patel\*

Received 3rd October 2008, Accepted 12th December 2008

First published as an Advance Article on the web 7th January 2009

DOI: 10.1039/b817285d

To enable several on-chip cell handling operations in a fused-silica substrate, small shallow micropores are radially embedded in larger deeper microchannels using an adaptation of single-level isotropic wet etching. By varying the distance between features on the photolithographic mask (mask distance), we can precisely control the overlap between two etch fronts and create a zero-thickness semi-elliptical micropore (*e.g.* 20  $\mu\text{m}$  wide, 6  $\mu\text{m}$  deep). Geometrical models derived from a hemispherical etch front show that micropore width and depth can be expressed as a function of mask distance and etch depth. These models are experimentally validated at different etch depths (25.03 and 29.78  $\mu\text{m}$ ) and for different configurations (point-to-point and point-to-edge). Good reproducibility confirms the validity of this approach to fabricate micropores with a desired size. To illustrate the wide range of cell handling operations enabled by micropores, we present three on-chip functionalities: continuous-flow particle concentration, immobilization of single cells, and picoliter droplet generation. (1) Using pressure differentials, particles are concentrated by removing the carrier fluid successively through a series of 44 shunts terminated by 31  $\mu\text{m}$  wide, 5  $\mu\text{m}$  deep micropores. Theoretical values for the concentration factor determined by a flow circuit model in conjunction with finite volume modeling are experimentally validated. (2) Flowing macrophages are individually trapped in 20  $\mu\text{m}$  wide, 6  $\mu\text{m}$  deep micropores by hydrodynamic confinement. The translocation of transcription factor NF- $\kappa$ B into the nucleus upon lipopolysaccharide stimulation is imaged by fluorescence microscopy. (3) Picoliter-sized droplets are generated at a 20  $\mu\text{m}$  wide, 7  $\mu\text{m}$  deep micropore T-junction in an oil stream for the encapsulation of individual *E. coli* bacteria cells.

## Introduction

The concept of micro total analysis systems (microTAS) introduced for chemicals in the early 1990s by Manz *et al.*<sup>1</sup> has been embraced by researchers in the emerging field of systems biology for studying the intra- and inter-cellular workings of a cell.<sup>2</sup> These microfluidic platforms enable multiplexed studies at the single-cell level in a controlled microenvironment with the inherent advantages of fast reaction times, small reagent consumption, and parallelization. The vast majority of these devices are focused on a single functionality or one basic operation (for a more comprehensive review see El-Ali *et al.*<sup>3</sup>). Only a handful of truly integrated cell-based microfluidic platforms with multiple components have been reported. Examples include a high-density array with hundreds of individually addressable cell chambers;<sup>4</sup> a device for single-cell manipulation, lysis, amino acid/protein labeling, and separation;<sup>5,6</sup> and a microfluidic chip to continuously monitor secreted insulin from multiple independent islets of Langerhans.<sup>7</sup> The majority of these multiplexed

platforms are fabricated from poly(dimethylsiloxane) (PDMS)<sup>8</sup> because microstructures such as valves,<sup>9</sup> weirs,<sup>10</sup> and micropores<sup>11</sup> can be easily embedded within a network of microfluidic channels.

Historically, silicon and glass have been the preferred substrate for the fabrication of microfluidic chips.<sup>12,13</sup> Despite the wide academic acceptance of PDMS-based microfluidic chips, glass remains an attractive alternative for many biological applications because of its large optical transition range (180–2500 nm); high resistance to mechanical stress, heat, and chemicals; high electric isolation; and high biocompatibility through its well-studied surface chemistry. Of the three major glass etching techniques—mechanical, dry, and wet—the most common microfabrication method practiced is isotropic wet etching. Well characterized in the literature,<sup>14,15</sup> this straightforward fabrication method uses a photolithography mask to define features on the surface of the wafer. Timed exposure to chemical etchants such as HF dissolves the Si–O–Si bonds in the glass isotropically, generating a D-shaped channel with a smooth surface and a constant depth. However, this technique is limited in that shallow structures (*i.e.* channels and weirs) are difficult to manufacture within larger channels without performing a multi-level wet etch or a combination of dry and wet etch—a costly and time-consuming operation because of the multiple masks and alignment steps needed between the different levels.

Sandia National Laboratories, PO Box 969, Livermore, CA, 94551, USA.  
E-mail: kdpatel@sandia.gov; Fax: +1 925 294 3020; Tel: +1 925 294 3737

† Electronic supplementary information (ESI) available: Sequence of 38 images showing 38 different etched channels in a point-to-point configuration with decreasing mask distance; video of continuous-flow particle concentration; and empirical determination of  $R_i + R_o$  and  $R_p$ . See DOI: 10.1039/b817285d

For on-chip cellular analysis, a simple fabrication technique for multi-depth microstructures in glass, analogous to PDMS-based platforms, is highly desired. Using single-level isotropic wet etch in glass, weir microstructures have been created within channels to retain multiple antibody-functionalized beads for immunoassays<sup>16,17</sup> and, more recently, to improve detection accuracy in flow cytometry.<sup>18</sup> In the present article, we show a unique adaptation of overlapping etch fronts in a single step to create multi-depth micropores within microfluidic channels for on-chip cell manipulation. In our approach, we precisely control the overlap of two etch fronts to create micropores of defined width and depth. We show that the measured micropore width and depth are in good agreement with simple geometrical models, which can be used to precisely tailor the size of the micropore to different applications. To illustrate this point, we present three on-chip functionalities enabled by micropores: continuous-flow concentration of particles, trapping of a single cell, and generation of picoliter-sized droplets.

## Materials and methods

### Chip design and fabrication

The chrome/quartz photomask (F62CQ6120; Photo Sciences) for the wet etch process is designed in L-Edit layout editor (Tanner Research). The two micropore designs created on the photomask are the point-to-point (p2p) and point-to-edge (p2e) geometries defined in Results and Discussion. The chips are custom-fabricated by Caliper Life Sciences using a proprietary processing recipe based on conventional photolithographic and wet etch protocols described previously.<sup>19</sup> Briefly, microchannels are isotropically etched in 0.70 mm thick fused-silica base wafers (Hoya Corporation) using a chrome hard mask and a stirred buffer oxide etch bath. The targeted etch depth is measured at multiple points on the wafer using a Tencor Alpha-Step profilometer calibrated on a daily basis. Fluid access holes (500  $\mu\text{m}$  diameter) are ultrasonically drilled into a cover wafer before being visually aligned and thermally bonded to the base wafer. The combined wafers are then diced with a wafer saw into individual  $22.6 \times 37.2$  mm chips. To be compatible with large numerical aperture (NA) microscope objective ( $\geq 1.4$ ), the base wafer was polished to a final thickness of 170  $\mu\text{m}$  using a proprietary lapping-polishing process (GM Associates) that resulted in a surface roughness of approximately 2 micro-inch (commercial grade finish 80/50 scratch/dig). Prior to each use, the channels are coated with a 4% BSA solution (A3059, Sigma) to prevent particle or cell adhesion to the walls.

### Chip packaging

A Delrin manifold with integrated Buna-N O-ring seals provides the interface between the microfluidic chip and fluid reservoirs.<sup>20</sup> Fluid is delivered to each port of the manifold through 1/32" O.D. 0.005" I.D. PEEK tubing (1576; Upchurch Scientific) and swaged in place with 1/32" TubeTite fittings (Labsmith). Screw-cap microcentrifuge tubes (2.0 mL – 89004-302; VWR) fitted with custom-machined caps serve as fluid reservoirs. The caps have two ports to allow the delivery of  $\text{N}_2$  gas to pressurize the headspace in the vial and push the fluid through a PEEK tube placed below the liquid level into the chip. All fluid reservoirs are

pressurized by individual electronic pressure control units (VSO-EP; Parker) to ensure precise control of pressure drops across the microfluidic chip. To maintain a temperature of 37  $^{\circ}\text{C}$  in the chip, two 35 W low inductance resistors (TCH35P4R70JE; Ohmite Mfg.) and a resistive thermal device sensor (RTD-830; Omega Engineering) were mounted to the compression frame with common heat-sink grease and powered by a temperature controller (CN132-12V; Omega Engineering). Flow rates are measured by Nano Flow sensors (N-565; Upchurch Scientific) calibrated against a syringe pump at room temperature prior to use. When measuring flow rates on the concentrator, care is taken to match the sensor readings and fluidic resistance by using an equal length of pre-cut PEEK tubing for each inlet and outlet, and positioning the inlet and outlet reservoirs at equal height. Flows for droplet generation were driven either by pressure controllers (Parker) or by syringe pumps (NE-500; New Era). When pressure controllers were used, upstream pressures were typically 70 kPa for the oil stream, with the aqueous pressure adjusted between 35–55 kPa. This configuration resulted in a  $\sim 1 \mu\text{L min}^{-1}$  oil flow rate, with generation of droplets from 20–80 Hz, and an aqueous/oil volumetric ratio between 1/5 and 1/20. When using syringe pumps, oil flow rates were typically 1–3  $\mu\text{L min}^{-1}$ , and aqueous flow rates were 0.2–0.6  $\mu\text{L min}^{-1}$ .

### Micropore metrology

Three microscopy techniques were used to characterize micropores: laser-scanning confocal fluorescence microscopy, field-emission scanning electron microscopy (FESEM), and brightfield microscopy. To image the micropore by laser-scanning confocal fluorescence microscopy (MRC1024ES; Biorad), a 100  $\mu\text{M}$  solution of fluorescein was flowed continuously throughout the chip while scanning to avoid photobleaching. A 60 $\times$  1.4 NA oil-immersion objective (Nikon) was used to image the chip through the polished 170  $\mu\text{m}$  glass surface. Sequential 0.5  $\mu\text{m}$  thick confocal images through a 30  $\mu\text{m}$  thick section were reconstructed into a three-dimensional rendering using 3D Doctor software (Able). To image the shape of the micropores by FESEM (6700; JEOL), a 20 to 30 nm thick carbon film was evaporated on an unbonded and undiced base wafer. The micropore width was measured by brightfield microscopy using a 100 $\times$  oil-immersion 1.40 NA objective (Olympus). The depth was measured with a XYZ automated microscope stage (MS2000; Applied Scientific Instrumentation) on a Nikon TE2000 microscope. To minimize operator error, multiple measurements were averaged together to produce the relationship between mask distance and micropore width or depth. All curves were fitted using a weighted least-squares Marquardt–Levenberg algorithm in Origin Pro 7.0 (OriginLab).

### Cell culture and reagents

The mouse macrophage cell line RAW 264.7 was grown on non-treated sterile flasks and maintained in growth media: 0.87X DMEM supplemented with 1 : 100 penicillin/streptomycin, 2 mM L-glutamine, 10% FBS, and 20 mM HEPES. The RG16 cell line stably expressing RelA-GFP was generated as described previously.<sup>21</sup> Macrophages were challenged with 1  $\mu\text{M}$  smooth *E. coli* lipopolysaccharide (L4524) in growth media. 10  $\mu\text{m}$



diameter polystyrene beads were purchased from Duke Scientific (4210A; Microgenics). For generation of water-in-oil microdroplets, two different formulations were used for the oil phase: (1) a blend of 60% (w/w) 20 cSt PDMS oil (378348) and 40% (w/w) Dow Corning Formulation Aid DC5225C; (2) mineral oil (M3516) with 4.5% (v/v) Span 80 (S6760), 0.4% (v/v) TWEEN 80 (P8074), and 0.05% (v/v) Triton X-100 (T9284). The aqueous phase was buffered with PBS. Bacteria encapsulation experiments were performed with fixed *E. coli* (K-12 strain) labeled with Alexa Fluor 488 (E-13231; Invitrogen), diluted to  $\sim 10^7$  cells mL $^{-1}$ . Prior to their first use, the glass microchannels were rendered hydrophobic by flushing the channels with a 5 mM solution of octadecyltrichlorosilane (AC14740; Acros Organics) in *n*-hexadecane (AC12046; Acros Organics) for 15 min. The coating solution was then flushed from the microchannels with pure *n*-hexadecane, followed by isopropanol for 5 min each. Unless specified, all reagents were purchased from Sigma-Aldrich.

## Results and discussion

### Micropore fabrication

Fused-silica is an amorphous material that wet etches isotropically. For example, a 10  $\mu$ m wide line on a photolithography mask with a 30  $\mu$ m etch depth will theoretically result in a 70  $\mu$ m wide, D-shaped channel (Fig. 1).<sup>14,15</sup> If mask features are separated from each other by a distance that is less than twice the etch depth, the isotropic wet etch will partially break through the channel sidewall to create a small opening where the two etch fronts first meet. Conceptually, two corners of a photolithographic mask that are separated by a distance of 56  $\mu$ m should generate a zero-thickness semi-circular micropore at the intersection of two D-shaped channels etched 30  $\mu$ m deep (Fig. 1). The location of a fabricated micropore was imaged by laser-scanning confocal microscopy in a quartz microfluidic chip filled

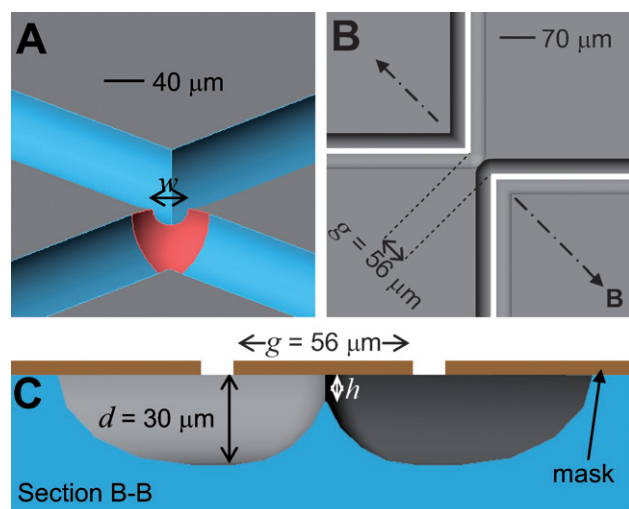


**Fig. 1** (A) CAD model of a micropore at an angled view for a point-to-point (p2p) configuration. (B) Top view of a wafer showing 30  $\mu$ m deep channels with overlapping corners. The openings of the photomask are shown in white with a 56  $\mu$ m mask distance. (C) Cross-sectional view along main axis defined in (B) illustrating the micropore after a 30  $\mu$ m etch depth.

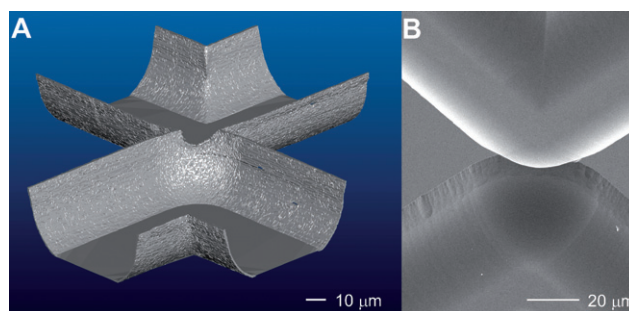


**Fig. 2** Imaged micropores fabricated by overlapping isotropic wet etch fronts. (A) 3D reconstruction from laser-scanning confocal microscopy. (B) SEM image angled at 40°.

with a 100  $\mu$ M solution of fluorescein. The 3D reconstruction of a stack of confocal images confirms the micropore location at the intersection of the two channel corners (Fig. 2A). In reality, the shape of the micropore is semi-elliptical rather than semi-circular, as shown by the angled SEM image of a 20  $\mu$ m wide, 6  $\mu$ m deep micropore (Fig. 2B).

The fabrication of such micropores within larger microfluidic channels using single-level isotropic wet etch can be tailored to a specific size demanded by cellular lab-on-a-chip applications. To design a micropore with the desired size, we developed a predictive geometrical model based on a hemispherical etch front. This model characterizes the dependence of the micropore width and depth to the distance separating the mask features (mask distance). The two configurations we considered on the photolithographic mask are point-to-point (Fig. 4A4) and point-to-edge (Fig. 4A6). In a point-to-point configuration, the mask distance is defined as the minimum distance between the tips of two opposing triangles, whereas in point-to-edge configuration, the minimum distance is between the tip of a triangle and a straight edge. From trigonometry, the micropore width  $w_{p2p}$  for the point-to-point configuration is given by

$$w_{p2p} = \sqrt{4d_{p2p}^2 - g_{p2p}^2} + b_{p2p} \quad (1)$$

where  $d$  is defined as the etch depth,  $g$  the mask distance, and  $b$  a systematic error. In the point-to-edge configuration, the micropore width  $w_{p2e}$  can be expressed as

$$w_{p2e} = 2\sqrt{(2d_{p2e} - g_{p2e})g_{p2e}} + b_{p2e} \quad (2)$$

For both configurations, the micropore depth  $h$  is given by

$$h = \frac{1}{2}\sqrt{4d^2 - g^2} + b \quad (3)$$

The validity of these geometrical models was tested by fabricating a series of micropores with mask distances changing by 1  $\mu$ m increments. The width and depth of each micropore were measured on an automated XYZ microscope stage using high-resolution brightfield microscopy. As an illustration of incrementally varying mask distance (67 to 30  $\mu$ m), 38 images of 25  $\mu$ m deep etched channels in a point-to-point configuration were assembled into a movie sequence (ESI Fig. S1†). This movie shows the etch fronts “kissing” at a 50  $\mu$ m mask distance—the theoretical expected value (twice the etch depth).

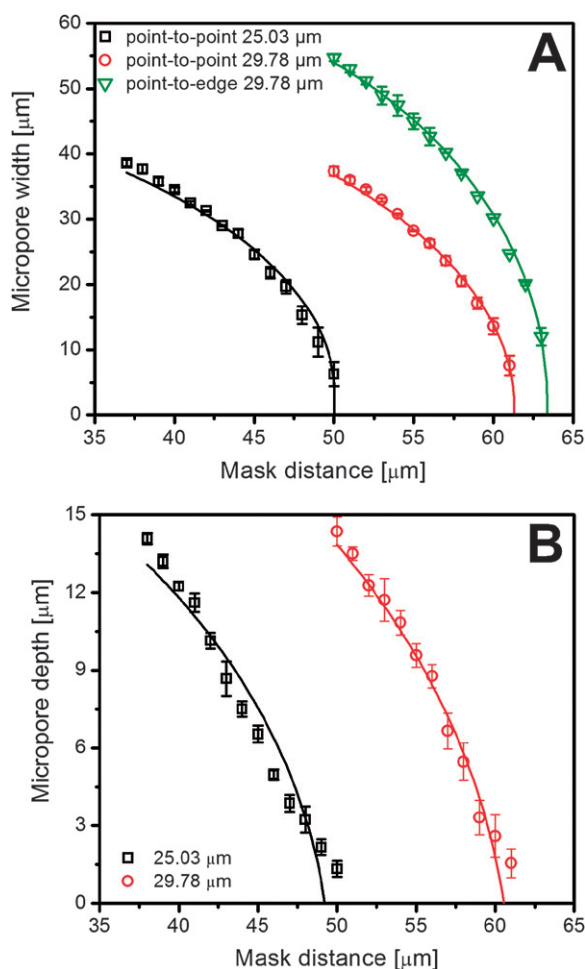


**Fig. 3** Micropore width and depth as a function of mask distance for two configurations and etch depths. (A) Micropore width for point-to-point configuration at 25.03 and 29.78  $\mu\text{m}$  etch depths and point-to-edge configuration at a 29.78  $\mu\text{m}$  etch depth. (B) Micropore depth for point-to-point configuration at a 25.03 and 29.78  $\mu\text{m}$  etch depths.

When  $w_{\text{p2p}}$  and  $w_{\text{p2e}}$  are plotted against the mask distance for an etch depth of 29.78  $\mu\text{m}$  (Fig. 3A), the point-to-edge configuration results in a larger micropore width since a circular etch front meets a flat etch front. Using eqn (1) and (2), we successfully fit  $w_{\text{p2p}}$  and  $w_{\text{p2e}}$  as a function of mask distance. The recovered etch depths from each fit ( $d_{\text{p2p}} = 30.6 \mu\text{m}$  and  $d_{\text{p2e}} = 31.7 \mu\text{m}$ ) are in good agreement with the profilometer-measured value (29.78  $\mu\text{m}$ , Table 1). To further validate our geometrical model at shallower etch depths,  $w_{\text{p2p}}$  is plotted against mask distance for a 25.03  $\mu\text{m}$  etch depth (Fig. 3A). In a similar analysis, but now using eqn (1), we recover a theoretical etch depth of  $d_{\text{p2p}} = 25.0 \mu\text{m}$  from the 25.03  $\mu\text{m}$  micropore series.

**Table 1** Fitting results for Fig. 3

	Micropore width			Micropore depth		
	$d/\mu\text{m}$	$b/\mu\text{m}$	$\chi^2_{\text{red}}$	$d/\mu\text{m}$	$b/\mu\text{m}$	$\chi^2_{\text{red}}$
Point-to-edge (29.78 $\mu\text{m}$ )	31.7	2.3	0.05	—	—	—
Point-to-point (29.78 $\mu\text{m}$ )	30.6	1.4	0.08	30.5	−3.6	0.28
Point-to-point (25.03 $\mu\text{m}$ )	25.0	3.4	1.9	24.9	−2.3	0.36

In Fig. 3B, the micropore depth  $h$  is plotted against mask distance for a 25.03 and 29.78  $\mu\text{m}$  etch depth series of micropores and fitted with eqn (3). The recovered etch depths from each fit ( $d = 24.9 \mu\text{m}$  and  $d = 30.5 \mu\text{m}$ ) are in good agreement with their measured values (25.03  $\mu\text{m}$  and 29.78  $\mu\text{m}$ ).

In Fig. 3A, the relationship between micropore width and mask distance is obviously nonlinear. For the micropore depth measurements (Fig. 3B), the range of mask distance probed is small and could be misconstrued as a linear function. When the mask distance is extrapolated to zero using eqn (3), the predicted micropore depth is similar to the measured etch depth (within 10%), which is not the case for a linear equation (over 200%). The range of mask distance probed in Fig. 3B is biased towards the highly sloped part of eqn (3).

Additionally, the misfit between theory and experiment has its greatest deviation for shallow micropores ( $<4 \mu\text{m}$ ), where the width-to-depth ratio is greater than 4. However, as the micropore becomes larger, there is a clear trend for this ratio to approach the theoretical value of a semicircle where  $w/h = 2$ . We believe that the breakdown between theory and experiment for these shallow micropores is a consequence of mask lift-off undercutting the wafer. Overall, the parameters determined for different geometrical models or at different etch depths are in good agreement with the measured values, demonstrating the validity of our geometrical models to predict the width and depth of micropores fabricated by overlapping isotropic wet etch fronts.

In addition to the geometrical equations discussed above, we investigated potential sources of systematic error originating from the photolithographic mask. A series of configurations with different inclusive angles ( $16^\circ$ – $16^\circ$ ,  $22^\circ$ – $22^\circ$ ,  $32^\circ$ – $32^\circ$ ,  $60^\circ$ – $60^\circ$ ,  $90^\circ$ – $90^\circ$ , and  $60^\circ$ – $180^\circ$ ) but separated from each other by a constant 60  $\mu\text{m}$  mask distance were designed (Fig. 4A). After a 30  $\mu\text{m}$  deep etch, the corresponding channels were imaged using brightfield microscopy (Fig. 4B). Despite a constant 60  $\mu\text{m}$  mask distance, the resulting overlap between the channels differs greatly for each design. For a  $16^\circ$ – $16^\circ$  configuration (Fig. 4B1), no overlap is observed, whereas, a micropore is formed for a  $90^\circ$ – $90^\circ$  configuration (Fig. 4B5). This discrepancy is a direct result of limited resolution in the photolithographic mask. For sharp angles, such as a  $16^\circ$  angle, the tip of the triangle is in reality filleted by the laser scribe during the manufacturing of the mask,

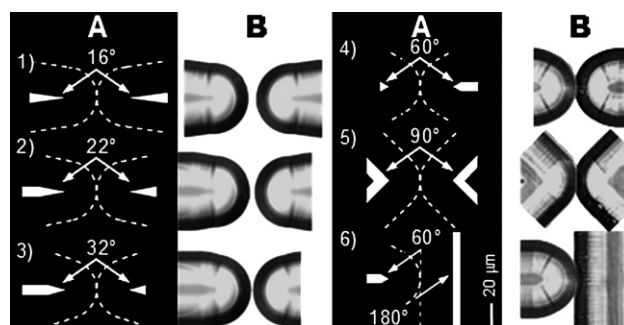


**Fig. 4** (A) Configurations with varying inclusive angles separated from each other by a constant 60  $\mu\text{m}$  mask distance (dashed white line theoretical etch front): 1)  $16^\circ$ – $16^\circ$ ; 2)  $22^\circ$ – $22^\circ$ ; 3)  $32^\circ$ – $32^\circ$ ; 4)  $60^\circ$ – $60^\circ$ ; 5)  $90^\circ$ – $90^\circ$ ; and 6)  $60^\circ$ – $180^\circ$ . (B) After a 30  $\mu\text{m}$  deep etch, the corresponding channels were imaged using brightfield microscopy.

thereby increasing the effective mask distance. As the total angle increases, the effective mask distance becomes closer to the design mask distance, thus increasing the extent of the overlap between the two etch fronts. When designing micropores, sharp angles ( $<60^\circ$ ) should be avoided as they introduce additional sources of error due to the limited resolution of the photolithographic mask.

The reproducibility of the micropore fabrication process was assessed for micropores within the same chip, between wafers processed simultaneously, and between wafers processed by different masks. In all cases, the maximum variation in the micropore widths never exceeded  $2\ \mu\text{m}$ . For instance, the average width for 10 micropores placed on the same chip was  $18.6 \pm 0.5\ \mu\text{m}$ . The good reproducibility of the fabrication process further supports the predictive capability of micropore fabricated by overlapping isotropic wet etch fronts.

The controlled fabrication of micropores and their incorporation within larger microfluidic channels facilitate the integration of advanced cell-based functionalities in a fused-silica chip. To demonstrate the usefulness of micropores, we present three specific on-chip functionalities where micropores play a key role: (1) continuous-flow particle concentration through a series of micropores; (2) immobilization of a single cell in a micropore; (3) encapsulation of bacteria in picoliter droplets generated at a micropore T-junction.

### Continuous-flow particle concentration through a series of micropores

In a microTAS device, each cell handling functionality is designed to operate optimally at a specific cell density. The ability to control the concentration of cells on-chip mitigates the “concentration mismatch” between integrated components. Additionally, a higher cell concentration enables shorter reaction times, reduced reagent volumes, and higher detection limits for certain applications. The continuous concentration of particles is generally preferred to a trap-and-release strategy when integrating with other on-chip components. Continuous-flow concentration techniques reported in the literature use electrokinetic effects.<sup>22,23</sup> Our approach is based on microsieving<sup>24</sup> constructed from multiple micropores. In this device, the carrier fluid containing the particle suspension is progressively withdrawn through a series of micropores, effectively concentrating the analyte.

The concentrator consists of two congruent, parallel channels (sample and waste) bridged by 44 shunts (Fig. 5). Each shunt is a  $330\ \mu\text{m}$  long channel terminated at each end by a  $31\ \mu\text{m}$  wide and  $5\ \mu\text{m}$  deep micropore in a point-to-edge configuration (inset of Fig. 5A). The concentrator was operated by applying a pressure differential,  $\Delta P$ , between the inlet and outlet fluid reservoirs and another pressure differential,  $\delta P$ , between the sample and waste legs. The induced transverse flow,  $\delta Q$ , from the sample leg to the waste leg in the concentrator is visualized in Fig. 5B, where small fractions of tracer dye are successively withdrawn through each shunt ( $\Delta P = 13.8\ \text{kPa}$ ,  $\delta P = 1.03\ \text{kPa}$ ). As an illustration of concentrating particles, the movie file given in ESI Fig. S2† shows simultaneously the entrance and exit of the concentrator. Smaller distances between successive polystyrene beads and smaller bead velocities at the exit demonstrates effective

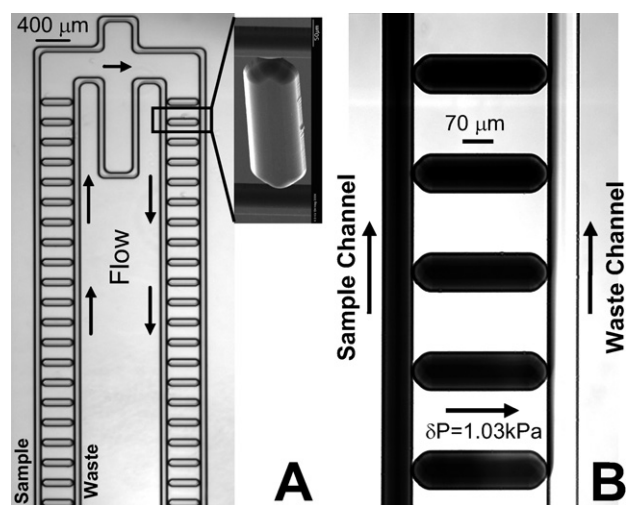


**Fig. 5** Micrographs of continuous-flow concentrator. (A) 44 shunt channels (42 shown) connect the sample (outer channel) to the waste (inner channel). Inset shows an SEM image of one shunt with two micropores at its extremities (rotated). (B) By applying pressure differentials ( $\Delta P = 13.8\ \text{kPa}$ ,  $\delta P = 1.03\ \text{kPa}$ ), small fractions of tracer dye are withdrawn from the sample to the waste through successive shunts.

concentration of the suspension of particles (initial concentration  $1 \times 10^5\ \text{beads mL}^{-1}$ ; final concentration  $\sim 4 \times 10^5\ \text{beads mL}^{-1}$ ).

The concentration factor that can be achieved for a given number of micropores can be predicted based on a simple flow circuit model (Fig. 6A). The model consists of seven flow resistors. Given the symmetry of the design, a pair of upstream resistors,  $R_i$ , connect the concentrator to the inlet reservoirs, a pair of downstream resistors,  $R_o$ , connect the concentrator to the outlet reservoirs, and a pair of resistors,  $R_c$ , represent the

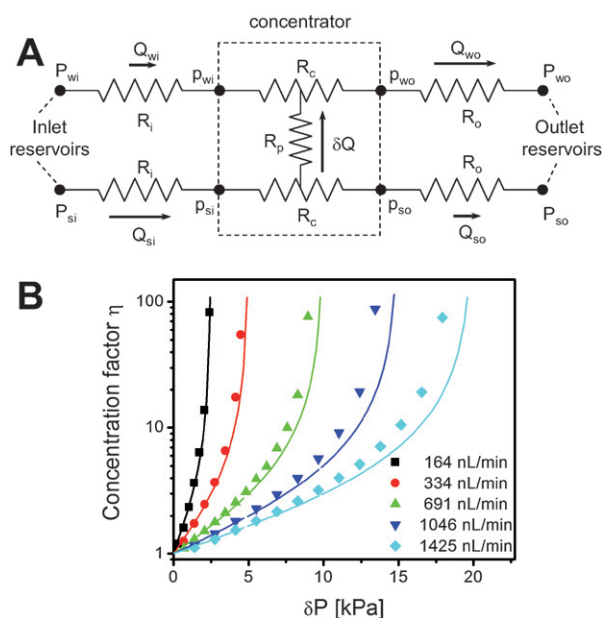


**Fig. 6** (A) A schematic of the flow circuit model for the concentrator, fluid reservoirs and connecting flow paths. (B) Predicted and measured concentration factors as a function of pressure differential  $\delta P$  for five different total flow rates  $\Sigma Q$ .



sample and waste legs of the concentrator. An additional resistor accounts for the 44 shunts connecting these two legs and has a combined resistance,  $R_p$ . The pressures in the reservoirs are designated as  $P_j$ , where the subscript  $j$  has values of  $si$  and  $wi$ , so and  $wo$  representing the sample and waste inlet reservoirs, and the sample and waste outlet reservoirs, respectively. The pressures at the entrance and exit of the concentrator are designated as  $p_j$ , where the subscript  $j$  takes on similar values and meanings as described above. Assuming fully developed steady flow, the relationships between the pressures, flow rates, and resistances are given by

$$P_{si} - p_{si} = R_i Q_{si} \quad (4a)$$

$$p_{so} - P_{so} = R_o Q_{so} \quad (4b)$$

$$P_{wi} - p_{wi} = R_i Q_{wi} \quad (4c)$$

$$p_{wo} - P_{wo} = R_o Q_{wo} \quad (4d)$$

The applied pressure differentials  $\delta P$  and  $\Delta P$  result in pressure differentials,  $\delta p_i$  and  $\delta p_o$ , between the sample and waste at the entrance and exit of the concentrator, respectively. This in turn drives the transverse flow,  $\delta Q$ , from the sample leg to the waste leg in the concentrator as given by eqn (5)

$$(\delta p_i + \delta p_o) = 2R_p \delta Q \quad (5)$$

where it is assumed that the driving pressure for this cross flow may be characterized by the average of the pressure differentials at the entrance and exit of the concentrator. From eqn (4),(5) and the definitions of  $\delta p_i = p_{si} - p_{wi}$  and  $\delta p_o = p_{so} - p_{wo}$ , the transverse flow,  $\delta Q$ , can be expressed as

$$\delta Q = \frac{2\delta P}{R_i + R_o + 2R_p} \quad (6)$$

Also, eqn (7) for the total flow,  $\Sigma Q = Q_{si} + Q_{wi} = Q_{so} + Q_{wo}$ , can be derived as

$$\Sigma Q = \frac{2\Delta P}{R_i + R_o + R_c} \quad (7)$$

For identical inlet and outlet channels, *i.e.*  $R_i = R_o$ , it can be shown that  $Q_{wo} = Q_{si}$ . Finally, the concentration factor defined as the ratio of the inlet sample flow rate to the outlet sample flow rate, *i.e.*  $\eta = Q_{si}/Q_{so}$ , is given by

$$\eta = \frac{\Sigma Q + \delta Q}{\Sigma Q - \delta Q} \quad (8)$$

The value for the concentrator leg resistance,  $R_c = 2.80 \text{ Pa nL min}^{-1}$ , was obtained using finite volume modeling as described previously.<sup>25</sup> A similar value is also obtained using an analytical expression<sup>26</sup> for flow through a rectangular channel. Values for the resistances  $R_i + R_o$  and  $R_p$  were determined empirically based on measurements of  $\delta Q$  and  $\Sigma Q$  for a wide range of  $\delta P$  and  $\Delta P$  values (ESI Fig. S3†). This data shows that  $2\Delta P/\Sigma Q = R_i + R_o + R_c$  is nearly independent of  $\delta P$  and  $\Delta P$  and equal to  $20.0 \text{ Pa nL min}^{-1}$ . Similarly, the data shows that  $2\delta P/\delta Q = R_i + R_o + 2R_p$  can be approximated as a constant,  $29.1 \text{ Pa nL min}^{-1}$ , if the data points at small  $\delta P$  are excluded. From these values and previously determined  $R_c$ , we obtain  $R_i + R_o = 17.2 \text{ Pa nL min}^{-1}$  and

$R_p = 5.95 \text{ Pa nL min}^{-1}$ . The value determined for  $R_i + R_o$  by this empirical method are in fair agreement with analytical estimates (flow through a circular channel<sup>26</sup>) based on the microchannels connecting the concentrator to the chip *via* holes, and the tubing connecting the chip to the fluid reservoirs. Also note that only this set of resistance values were used in eqn (6)–(8) to make predictions for the concentration factor over a wide range of operating conditions.

The concentration factor,  $\eta$ , was experimentally determined by measuring flow rates at the sample and waste outlets using two matched flow sensors. Both measured and predicted concentration factors are plotted as a function of the pressure differential  $\delta P$  for five different total flow rates  $\Sigma Q$  (Fig. 6B). For a given  $\delta P$ , the measured concentration factors become larger than the predicted values, and this difference increases with increasing  $\delta P$ . This systematic discrepancy can be attributed to the variation in  $2\delta P/\delta Q = R_i + R_o + 2R_p$ , which decreases with increasing  $\delta P$  according to the experimental data (ESI Fig. S3B†), while it is assumed to be a constant in the model. If this variation was accounted for in the model, the predictions would be in better agreement with the experiments. Nevertheless, the predictions for the concentration factor obtained from eqn (6)–(8) are overall in good agreement with the measured experimental data. From a practical point-of-view, concentration factors above 10 are not realistic since a significant fraction of liquid is withdrawn from the sample by each shunt. In this case, particles could potentially clog the micropores, which in turn increases the pressure differential  $\delta P$  on the remaining shunts thus increasing their likelihood of also being clogged.

The capability to precisely control the dimensions of the micropores is key to the performance of the concentrator for a number of reasons. First, the micropores must be very small to create a large flow resistance ( $R_p$ ) so that the pressures in the waste and sample channels do not equilibrate and a transverse flow is maintained. Second, while the design fabricated here performed well, an optimized design would require that the micropores have a size that depends on their location in the concentrator. That is, based on detailed finite volume modeling the pressure difference across the micropores was not the same for all, rather, it was larger for those micropores located near the inlet and outlet of the concentrator. Consequently, a design that results in the same flow rate through every micropore requires that those micropores be smaller than the micropores in the middle of the concentrator. The flow rate through a micropore is sensitive to its size and shape so a precision fabrication method is essential for an optimized design.

### Immobilization of a single cell in a micropore

Single-cell analysis, a key approach for future biological discoveries, requires revolutionary tools to transport, immobilize, and image individual cells efficiently. Several microfluidic techniques have been developed to transport and immobilize single cells in an array, including: (1) dielectrophoretic trapping, which confines cells in a potential well created by electrodes but involves complicated chip fabrication processes;<sup>27,28</sup> (2) holographic optical trapping, limited by low throughput<sup>29</sup> and by the induced photodamage on the cell after an extended period of time;<sup>30</sup> (3) microwell trapping, characterized by a random and

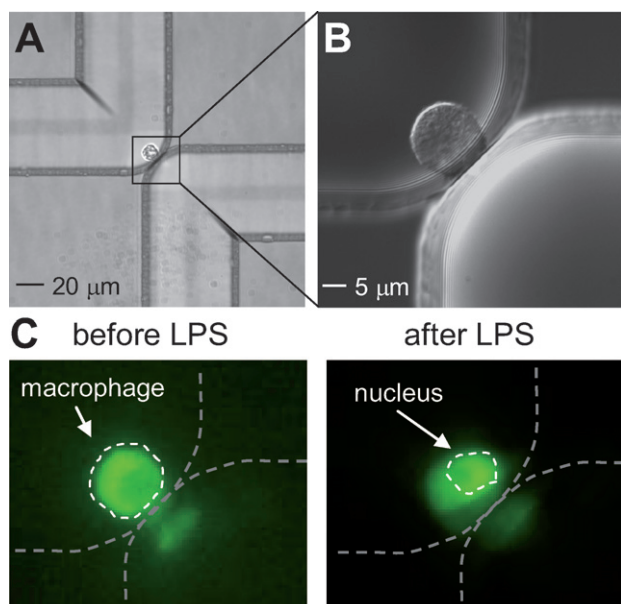


**Fig. 7** Single mouse macrophage cell trapped by a micropore. (A) Imaged by a  $40\times 0.60$  NA objective. (B) Imaged by differential interference microscopy using a  $60\times 1.42$  NA oil-immersion objective. (C) Nuclear translocation of NF- $\kappa$ B in a macrophage cell trapped by a micropore. GFP-RelA is located in the cytosol prior to activation (before LPS). GFP-RelA is located in the nucleus after a 30 min challenge (after LPS).

slow cell loading step given its reliance on gravitational forces.<sup>31,32</sup> None of these techniques rivals the inherent simplicity and efficiency of hydrodynamic confinement. In this approach, a fraction of the cells and media flow towards an unoccupied trap. Once a single cell is trapped in the cavity, it acts as a partial plug, dramatically increasing the fluidic resistance along this path and redirecting the rest of the sample away from the occupied trap. In this configuration, the trapping of cells is directional as opposed to random; moreover, for defined trap dimensions, occupancy of a single cell per trap can be achieved. In previous reports, the cavity has been a dam structure,<sup>33</sup> a  $2$  by  $2\ \mu\text{m}$  cross-section channel,<sup>34</sup> or a  $2\ \mu\text{m}$  gap.<sup>10</sup> In our design, the trap consists of a micropore formed by folding a  $70\ \mu\text{m}$  wide channel such that two of its corners are overlapping (Fig. 7A).

A single mouse macrophage cell immobilized in a  $20\ \mu\text{m}$  wide and  $6\ \mu\text{m}$  deep micropore is imaged by Nomarski differential interference contrast microscopy (Fig. 7B). As an example of assays on single cells trapped by micropores, we imaged the nuclear translocation of nuclear factor kappa-B (NF- $\kappa$ B), a multi-subunit transcription factor that controls many inflammation-related genes in mouse macrophages. This translocation is induced by lipopolysaccharide (LPS), a component of Gram-negative bacterial cell walls and a potent stimulator of macrophages. Nuclear translocation of NF- $\kappa$ B was monitored by tagging its RelA subunit with GFP in a stably transfected macrophage cell line. Fig. 7C shows the fluorescent images of RelA for a representative single macrophage cell captured in a micropore. In order to reduce fluorescent background from growth media, each captured cell was imaged in PBS before being incubated in growth media with  $1\ \mu\text{M}$  LPS for 30 min at  $37\ ^\circ\text{C}$ .

After the LPS challenge, growth media was replaced by PBS and the presence of NF- $\kappa$ B in the nucleus was detected by epi-fluorescence microscopy. A slight image distortion is observed at the micropore due to the optical interference of the micropore curvature with the fluorescent images of the cell. This distortion can be avoided by imaging the cell from the opposite side of the micropore, where the quartz has a flat surface. By immobilizing a flowing single cell at a desired location, we showed that these micropores embedded into channels represent a simple and practical approach for cell manipulation in a microTAS device.

### Encapsulation of bacteria in picoliter droplets generated at a micropore T-junction

Two-phase droplet-based microfluidic systems have received significant attention for encapsulation of individual cells for high-throughput assays.<sup>35–39</sup> Two geometries are common for continuous generation of picoliter- or nanoliter-sized droplets in microfluidic chips: the flow-focusing geometry, and the T-junction. In a typical T-junction fabricated by a single-level isotropic wet etch in glass, the width of the dispersed-phase channel is at least twice the depth of the channel. When the width of both of the dispersed-phase and continuous-phase channels are similar, droplets tend to be elongated, and occupy nearly the entire channel width, with only a thin film of the continuous phase wetting the channel walls (so-called “plugs” or “confined” droplets). “Unconfined” droplets are more typically obtained when the dispersed-phase channel is significantly smaller than the continuous-phase channel.<sup>40</sup>

To achieve smaller droplets for a given channel width, we used a point-to-edge configuration to create a micropore T-junction.

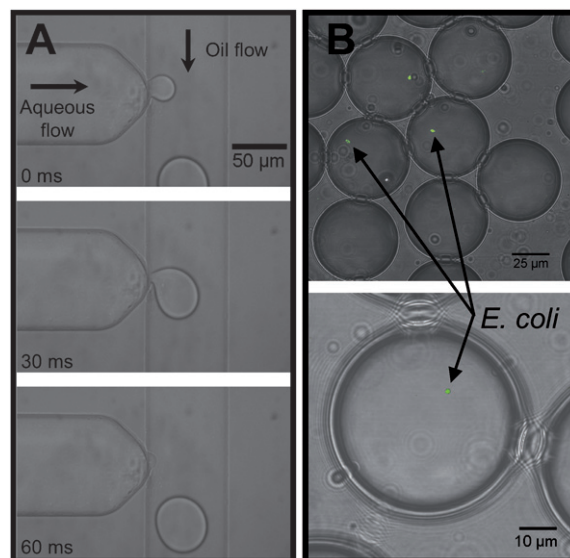


**Fig. 8** (A) Formation and breakoff of an aqueous droplet into a silicone oil stream at a  $20\ \mu\text{m}$  wide,  $7\ \mu\text{m}$  deep micropore T-junction. (B) Laser-scanning confocal images of fixed, Alexa Fluor 488-labeled *E. coli* cells encapsulated on-chip in aqueous droplets generated at a micropore T-junction, and spotted onto a coverslip for imaging. The images are composites of transmitted light and fluorescence images acquired simultaneously with a  $60\times 1.4$  NA objective. Cell boundaries appear blurry due to Brownian motion during the laser-scanning time.



We thus overcome traditional limitations by shrinking the size of the channel intersection without decreasing the etch depth, which would otherwise lead to significantly higher pressure drop throughout the chip. Fig. 8A illustrates formation and breakoff of an aqueous droplet in an immiscible oil using a 20  $\mu\text{m}$  wide, 7  $\mu\text{m}$  deep micropore T-junction in a 25.03  $\mu\text{m}$  deep channel. The reduced area of intersection between the dispersed (aqueous) and continuous (oil) streams causes the droplet to be pinched to a narrow “neck” prior to breakoff, without significant interaction with the side walls of the microchannel. In this example, the droplet has an apparent diameter in the channel of  $\sim 45 \mu\text{m}$ , and is partially compressed vertically in the 25  $\mu\text{m}$  deep channel.

We have used our micropore droplet generator to encapsulate bacteria, as a first step to performing diagnostic assays such as quantitative PCR on individual cells.<sup>41</sup> An aqueous suspension of fixed, fluorescently labeled *E. coli* was fed into an oil stream through a micropore T-junction. The droplets were collected off chip, and imaged by laser-scanning confocal microscopy on a coverslip (Fig. 8B). On the coverslip, the droplets presumably adopt a spherical configuration, with a typical diameter of  $\sim 50 \mu\text{m}$ , for a volume of  $\sim 65 \text{ pL}$ . A single bacterial genome in such a droplet has an effective concentration of 25 fM, which is two orders of magnitude higher than would be obtained in microfabricated nanoliter reactors previously reported for “digital PCR” assays on individual microbes.<sup>42</sup>

## Conclusions

We present a novel approach for creating micropores embedded in microfluidic channels using overlapping isotropic wet etch fronts. This simple approach enables additional on-chip cell handling operations, without resorting to multi-level etching or other laborious fabrication techniques that are otherwise needed to produce multi-depth structures in glass chips. Using our predictive geometrical models, we implemented three different micropore sizes and configurations to illustrate just three of the possible on-chip cell functionalities micropores can offer (particle concentration, single-cell trapping, and picoliter droplet generation). Other possible adaptations include 3D hydrodynamic focusing (albeit at high Reynolds numbers), patch-clamp measurements, and sieving strategies. Each application requires precise control over the micropore size to achieve predictable, reproducible results. We have shown that the micropore fabrication process is reproducible from one device to the next, and our geometric model allows micropores of specific sizes to be designed with confidence. In summary, fabricating multiple micropores with different sizes in one simple step is a significant advancement in overcoming the barriers for using fused-silica microTAS devices for sophisticated cell-based assays.

## Acknowledgements

The authors would like to thank M. McReynolds from Caliper Life Sciences, N. Y.-C. Yang, J. M. Chames, M. R. Claudnic, and D. D. Yee for their assistance. We also appreciate inspiring discussions with N. Srivastava and D. E. Huber. This research was fully supported by the Laboratory Directed Research and Development Program at Sandia National Laboratories. Sandia is a multiprogram laboratory operated by Sandia Corporation,

a Lockheed Martin Company, for the United States Department of Energy's National Nuclear Security Administration under contract DE-AC04-94AL85000.

## References

- 1 A. Manz, N. Graber and H. M. Widmer, *Sens. Actuators, B*, 1990, **1**, 244–248.
- 2 D. N. Breslauer, P. J. Lee and L. P. Lee, *Mol. BioSyst.*, 2006, **2**, 97–112.
- 3 J. El-Ali, P. K. Sorger and K. F. Jensen, *Nature*, 2006, **442**, 403–411.
- 4 T. Thorsen, S. J. Maerkl and S. R. Quake, *Science*, 2002, **298**, 580–584.
- 5 H. K. Wu, A. Wheeler and R. N. Zare, *Proc. Natl. Acad. Sci. U. S. A.*, 2004, **101**, 12809–12813.
- 6 B. Huang, H. K. Wu, D. Bhaya, A. Grossman, S. Granier, B. K. Kobilka and R. N. Zare, *Science*, 2007, **315**, 81–84.
- 7 J. F. Dishinger and R. T. Kennedy, *Anal. Chem.*, 2007, **79**, 947–954.
- 8 D. C. Duffy, J. C. McDonald, O. J. A. Schueller and G. M. Whitesides, *Anal. Chem.*, 1998, **70**, 4974–4984.
- 9 M. A. Unger, H. P. Chou, T. Thorsen, A. Scherer and S. R. Quake, *Science*, 2000, **288**, 113–116.
- 10 D. Di Carlo, N. Aghdam and L. P. Lee, *Anal. Chem.*, 2006, **78**, 4925–4930.
- 11 J. Seo, C. Ionescu-Zanetti, J. Diamond, R. Lal and L. P. Lee, *Appl. Phys. Lett.*, 2004, **84**, 1973–1975.
- 12 T. McCreedy, *TrAC, Trends Anal. Chem.*, 2000, **19**, 396–401.
- 13 B. Ziaie, A. Baldi, M. Lei, Y. D. Gu and R. A. Siegel, *Adv. Drug Delivery Rev.*, 2004, **56**, 145–172.
- 14 S. C. Jacobson, A. W. Moore and J. M. Ramsey, *Anal. Chem.*, 1995, **67**, 2059–2063.
- 15 M. J. Madou, *Fundamentals of microfabrication*, CRC Press, Boca Raton, FL, 1997.
- 16 K. Sato, M. Yamanaka, T. Hagino, M. Tokeshi, H. Kimura and T. Kitamori, *Lab Chip*, 2004, **4**, 570–575.
- 17 A. J. Haes, A. Terray and G. E. Collins, *Anal. Chem.*, 2006, **78**, 8412–8420.
- 18 L. M. Fu, C. H. Tsai and C. H. Lin, *Electrophoresis*, 2008, **29**, 1874–1880.
- 19 D. J. Throckmorton, T. J. Shepodd and A. K. Singh, *Anal. Chem.*, 2002, **74**, 784–789.
- 20 R. F. Renzi, J. Stamps, B. A. Horn, S. Ferko, V. A. VanderNoot, J. A. A. West, R. Crocker, B. Wiedenman, D. Yee and J. A. Fruetel, *Anal. Chem.*, 2005, **77**, 435–441.
- 21 T. D. Perroud, J. N. Kaiser, J. C. Sy, T. W. Lane, C. S. Branda, A. K. Singh and K. D. Patel, *Anal. Chem.*, 2008, **80**, 6365–6372.
- 22 C. R. Cabrera and P. Yager, *Electrophoresis*, 2001, **22**, 355–362.
- 23 L. M. Barrett, A. J. Skulan, A. K. Singh, E. B. Cummings and G. J. Fiechtner, *Anal. Chem.*, 2005, **77**, 6798–6804.
- 24 P. Sethu, A. Sin and M. Toner, *Lab Chip*, 2006, **6**, 83–89.
- 25 C. K. Harnett, J. Templeton, K. A. Dunphy-Guzman, Y. M. Senousy and M. P. Kanouff, *Lab Chip*, 2008, **8**, 565–572.
- 26 F. M. White, *Viscous Fluid Flow*, McGraw-Hill, New York, NY, 2006.
- 27 J. Voldman, M. L. Gray, M. Toner and M. A. Schmidt, *Anal. Chem.*, 2002, **74**, 3984–3990.
- 28 A. B. Fuchs, A. Romani, D. Freida, G. Medoro, M. Abonnenc, L. Altomare, I. Chartier, D. Guergour, C. Villiers, P. N. Marche, M. Tartagni, R. Guerrieri, F. Chatelain and N. Manaresi, *Lab Chip*, 2006, **6**, 121–126.
- 29 R. A. Flynn, A. L. Birkbeck, M. Gross, M. Ozkan, B. Shao, M. M. Wang and S. C. Esener, *Sens. Actuators, B*, 2002, **87**, 239–243.
- 30 K. C. Neuman, E. H. Chadd, G. F. Liou, K. Bergman and S. M. Block, *Biophys. J.*, 1999, **77**, 2856–2863.
- 31 I. Inoue, Y. Wakamoto, H. Moriguchi, K. Okano and K. Yasuda, *Lab Chip*, 2001, **1**, 50–55.
- 32 M. Deutsch, A. Deutsch, O. Shirihai, I. Hurevich, E. Afrimzon, Y. Shafran and N. Zurgil, *Lab Chip*, 2006, **6**, 995–1000.
- 33 M. S. Yang, C. W. Li and J. Yang, *Anal. Chem.*, 2002, **74**, 3991–4001.
- 34 P. J. Lee, P. J. Hung, R. Shaw, L. Jan and L. P. Lee, *Appl. Phys. Lett.*, 2005, **86**, 223902–223901.
- 35 J. Q. Boedicker, L. Li, T. R. Kline and R. F. Ismagilov, *Lab Chip*, 2008, **8**, 1265–1272.
- 36 M. Chabert and J. L. Viovy, *Proc. Natl. Acad. Sci. U. S. A.*, 2008, **105**, 3191–3196.

- 
- 37 J. F. Edd, D. Di Carlo, K. J. Humphry, S. Koster, D. Irimia, D. A. Weitz and M. Toner, *Lab Chip*, 2008, **8**, 1262–1264.
- 38 M. Y. He, J. S. Edgar, G. D. M. Jeffries, R. M. Lorenz, J. P. Shelby and D. T. Chiu, *Anal. Chem.*, 2005, **77**, 1539–1544.
- 39 A. Huebner, L. F. Olguin, D. Bratton, G. Whyte, W. T. S. Huck, A. J. de Mello, J. B. Edel, C. Abell and F. Hollfelder, *Anal. Chem.*, 2008, **80**, 3890–3896.
- 40 G. F. Christopher and S. L. Anna, *J. Phys. D: Appl. Phys.*, 2007, **40**, R319–R336.
- 41 N. R. Beer, B. J. Hindson, E. K. Wheeler, S. B. Hall, K. A. Rose, I. M. Kennedy and B. W. Colston, *Anal. Chem.*, 2007, **79**, 8471–8475.
- 42 E. A. Ottesen, J. W. Hong, S. R. Quake and J. R. Leadbetter, *Science*, 2006, **314**, 1464–1467.